

Computer-Vision-Based Approach to Classify and Quantify Flaws in Li-Ion Electrodes

Sohrab R. Daemi, Chun Tan, Thomas G. Tranter, Thomas M. M. Heenan, Aaron Wade, Luis Salinas-Farran, Alice V. Llewellyn, Xuekun Lu, Alessia Matruglio, Daniel J.L. Brett, Rhodri Jervis,* and Paul R. Shearing*

X-ray computed tomography (X-ray CT) is a non-destructive characterization technique that in recent years has been adopted to study the microstructure of battery electrodes. However, the often manual and laborious data analysis process hinders the extraction of useful metrics that can ultimately inform the mechanisms behind cycle life degradation. This work presents a novel approach that combines two convolutional neural networks to first locate and segment each particle in a nano-CT LiNiMnCoO₂ (NMC) electrode dataset, and successively classifies each particle according to the presence of flaws or cracks within its internal structure. Metrics extracted from the computer vision segmentation are validated with respect to traditional threshold-based segmentation, confirming that flawed particles are correctly identified as single entities. Successively, slices from each particle are analyzed by a pre-trained classifier to detect the presence of flaws or cracks. The models are used to quantify microstructural evolution in uncycled and cycled NMC811 electrodes, as well as the number of flawed particles in a NMC622 electrode. As a proof-of-concept, a 3-phase segmentation is also presented, whereby each individual flaw is segmented as a separate pixel label. It is anticipated that this analysis pipeline will be widely used in the field of battery research and beyond.

central position in our future.^[1] Over the last few decades, Li-ion batteries have emerged as the technology of choice for a range of portable energy storage solutions due to their high energy densities and capacities. For full implementation of these devices in stationary grid applications or electric vehicles, improvements are required in terms of cycle life, power and energy densities, safety, and cost.^[2] Li-ion batteries operate via a “rocking chair” mechanism, where Li-ions travel between a cathode and an anode during charge and discharge operations.^[3] More specifically, most cathodes are formed by layered transition metal oxides that host Li-ions between different layers.^[4] As cells are charged with the application of an electrical current, Li-ions de-intercalate from the cathode and traverse a liquid electrolyte to the anode, usually a carbonaceous material.^[5] During discharge, the ions migrate back, releasing the stored electrical energy in an external circuit,

1. Introduction

As the world is moving toward increased electrification of the energy grid and automotive fleet due to environmental concerns, robust energy storage devices are increasingly taking a

accompanied by redox changes in the electrode materials. The complex electrode microstructures which are characteristically found in Li-ion batteries play a pivotal role in determining the electrochemical performance: there is a synergistic effect; not only can different cycling regimes influence the morphological evolution of the constituting particles, but the morphology of the particles themselves can have a determining effect on cycle life or rate capability of the batteries they are employed in. For example, internal stresses may arise due to the repeated intercalation of Li-ions during cycling, resulting in micro-, and nano-scale cracks throughout the particle volume.^[6]

Different techniques such as focused-ion beam scanning electron microscopy (FIB-SEM), atomic force microscopy (AFM), and X-ray computed tomography (X-ray CT) have been employed to further elucidate the intrinsic link between electrode morphology and battery performance.^[7–11] X-ray CT has garnered particular interest due to its non-destructive nature and multi-scale and in situ capabilities. The technique involves collecting 2D radiographs at different angular rotations and reconstructing these to 3D datasets whereby the resulting attenuation of the X-ray is inversely proportional to the contrast of the resulting image.^[12] After reconstruction, each voxel contained in the image is segmented by assigning it to the phase of interest according to its grayscale value. For example, less dense


S. R. Daemi, C. Tan, T. G. Tranter, T. M. M. Heenan, A. Wade, L. Salinas-Farran, A. V. Llewellyn, X. Lu, A. Matruglio, D. J. L. Brett, R. Jervis, P. R. Shearing

Electrochemical Innovation Lab
Department of Chemical Engineering
University College London
London WC1E 7JE, UK

E-mail: rhodri.jervis@ucl.ac.uk; p.shearing@ucl.ac.uk

T. Heenan, A. Wade, A. V. Llewellyn, D. J. L. Brett, R. Jervis, P. R. Shearing
The Faraday Institution

Quad One
Harwell Science and Innovation Campus
Didcot OX11 0RA, UK

 The ORCID identification number(s) for the author(s) of this article can be found under <https://doi.org/10.1002/smt.202200887>.

© 2022 The Authors. Small Methods published by Wiley-VCH GmbH. This is an open access article under the terms of the Creative Commons Attribution License, which permits use, distribution and reproduction in any medium, provided the original work is properly cited.

DOI: 10.1002/smt.202200887

materials such as air or the carbon binder domain (CBD), will appear darker, whereas denser materials such as transition metal oxides appear lighter. This process allows quantifying different morphological characteristics and phenomena related to battery performance and electrode degradation.

Flaws and cracks can form in the active material particles as a result of synthesis, electrode manufacture or cell cycling.^[13–15] Fracture of the active materials contained in electrodes is one of the main factors responsible for battery capacity fading: cyclical cracking eventually causes the active material to isolate and lose contact with the ionic and/or electronic pathways necessary for battery operation.^[16] Furthermore, cracking exposes fresh surfaces of active materials that continuously react with the electrolyte, reducing cycling efficiency and accelerating electrolyte consumption.^[17] In order to characterize microstructural degradation or quantify the amount of new surfaces that are generated as a result, it is critical to accurately segment the dataset in 3D. However, during the segmentation process, separating such flaws from the surrounding pore space or CBD is a tedious task due to their common low attenuation properties that result in poor contrast. While manual segmentation and classification approaches can be used to separate and segment flawed particles, these are often impossible to carry out on large data sets and can contain many human errors due to the intricate microstructures, large number of particles and 3D nature of the data.

Machine learning-based techniques are gaining considerable interest for studying different facets of battery operation. For example, CNNs have recently been used for battery health prediction and crack detection in labelled data.^[18–22] While CV approaches show great promise as an alternative route to analyze image data, their application to segmentation of 3D tomographic data remains limited. Two notable examples used semantic segmentation for an accurate multi-phase electrode segmentation and object recognition and, semantic segmentation of flawed particles.^[23,24]

Building on these previous studies, we propose, for the first time to the authors' knowledge, an automated process to segment and classify each particle in NMC-based Li-ion cathode nano-CT datasets. By combining the established instance segmentation package Mask R-CNN with a simple VGG16 classifier, we are able to automatically segment the active material phase in 3D nano-CT datasets, detect each individual particle and classify it according to the presence of flaws or cracks within its microstructure.^[25] Furthermore a 3-phase segmentation of each particle can be obtained that shows the particle, external pore/CBD and internal flaw or crack as distinct phases. To improve the ability of the model to generalize on unseen data, an algorithm is provided that can automatically generate machine readable Microsoft Common Objects in Context (MS COCO) annotations from previously segmented data. This exponentially increases the number of single particle instances that can be used for training or validation.

As a proof of concept, the approach is applied to several battery tomogram datasets containing a multitude of flaws or cracks as a result of synthesis and cycling, that were previously unseen by the model. Excluding the time required to prepare data for model training, the automated nature of the process allows for a full electrode segmentation and particle classification in just a few hours, depending on resolution and

dataset size. This is a stark contrast from any manual threshold-based approach, where the accurate segmentation of a few individual particles can take a considerable amount of time. For simplicity, we will refer to particles containing internal voids, flaws, or cracks as flawed, unless specified otherwise.

We believe the overall process, with future improvements in detection and segmentation accuracy, will be adaptable to a multitude of case studies in the field of Li-ion research and beyond. With the increased prevalence of X-ray CT as an analysis tool for Li-ion batteries, and the requirement for ever larger analysis volumes and datasets in order to provide statistical significance to their analysis, inevitably, some form of automation in the segmentation and analysis of the data will occur. Coupled with this, acquisition times for CT data sets are ever-decreasing in both lab and synchrotron experiments, to the extent that CT is becoming a viable tool for quality assurance in battery manufacturing. The sheer volume of data being generated requires accurate automated analysis such as that which we propose here to extract useful information that enables rapid diagnosis of battery electrode microstructures.

2. Results

2.1. Automated Label Generation

The proposed segmentation and classification pipeline is presented in **Figure 1**.

MS COCO dataset is a large-scale collection of images divided in 91 common object categories.^[26] Overall, the dataset contains 2 500 000 labeled instances in 328 000 images. These images are accompanied by a standardized format of categorizing and annotating each object in the image, along with exact bounding box and segmentation coordinates. To train custom datasets, custom categories and segmentations can be created in COCO-style annotations using freely available tools such as VGG Image Annotator (VIA).^[27] Here, image outlines can be selected via manual tools and assigned to categories of interest. While this method is undoubtedly effective when dealing with a small number of training sets, manually labeling the images is laborious and time-consuming, and is therefore unsuitable for routine segmentation of large data volumes.

An alternative method is proposed, whereby labels are automatically generated from each 2D slice part of a 3D dataset. The code is available in our public repository. As an input, the code takes grayscale images and their respective binarized label fields as 2D stacks of 3D datasets and automatically divides the images into training and validation sets according to the percentage decided by the user. Binary segmentations can be produced with automated methods that are more time-efficient such as watershed or thresholding. Further manual optimization of the segmentation also has to be carried out to ensure that cracks and flaws are identified as part of the solid or particle phase: the training data needs to resemble the desired outcome as much as possible for the best result. Due to the 2D nature of the Mask R-CNN training, each separate 3D particle can be considered as a collection of 2D instances that will be fed independently to the model. As a result, the

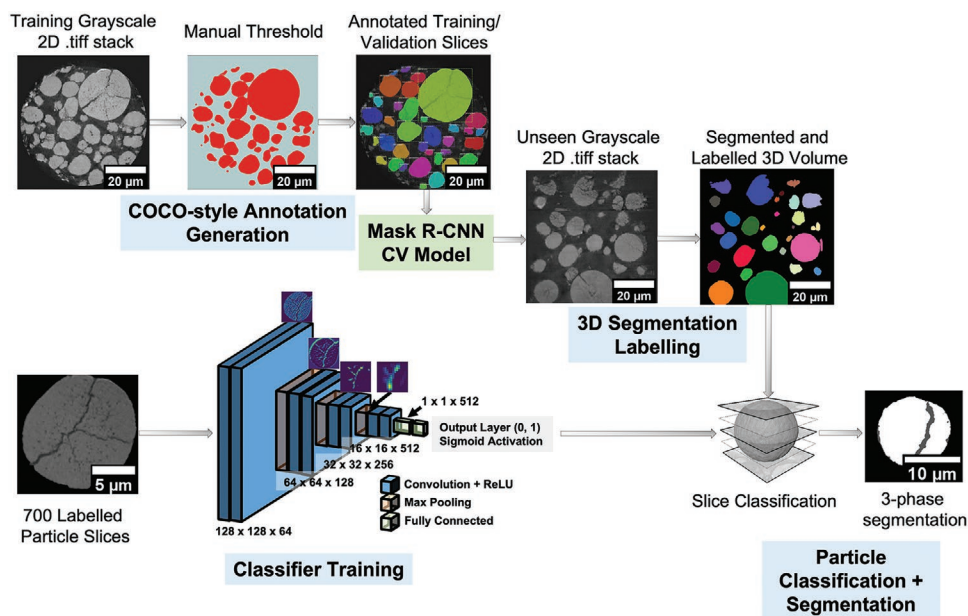


Figure 1. The proposed pipeline for generating annotations, segmenting, and classifying particles from a nano-CT dataset. COCO-style annotations were used to train a Mask R-CNN model which successively isolated individual particles in 3D nano-CT datasets. Separately, a classifier was trained to recognize whether a particle contains a crack or flaw. Each individual particle from the segmentation was then classified according to the presence of a crack or flaw and segmented in three phases.

number of training or validation instances were exponentially higher than what is achieved manually using VIA for example, but with comparable, if not shorter, preparation times. Consequently, from five datasets comprised of around 1640 slices in the XY axis, a total of over 49 000 single instance particles were obtained. As neighboring slices may contain similar features, the augmentation discussed in the methodology section introduces significant differences leading to an improved ability of the model to generalize on unseen data. An example of such augmentation is presented in Figure S3, Supporting Information.

2.2. Computer Vision Segmentation Validation

To evaluate the performance of the segmentation network, several metrics were extracted from the 2D slice segmentations as presented in Figure 2. Two different electrodes from the training sets were compared: having the ground truth segmentation previously generated with thresholding enables plotting the Precisions-Recalls curve and calculating the mean average precision (mAP). As a default in the Mask R-CNN package, these metrics were calculated at an intersection over union (IoU) of 50% (mAP@IoU50). The mAP@IoU50 denotes the mean average precision calculated where there is an overlap of at least 50% between the detected bounding boxes and the ground truth segmentation. The precision of a classification model indicates what percentage of predictions is correctly identified on all predictions, while the recall describes the percentage of correctly annotated objects in the ground truth. Two datasets were chosen, namely one without flawed particles, and one with, as presented in Figures 2a,b respectively.

As presented in the Precisions–Recalls curve for an individual slice extracted from each dataset, most particles are detected correctly by the model. However, a slight decrease in recall is present for the flawed electrode. This is also shown in Figure 2b as the model struggled to recognize particles with uneven morphologies due to cracking or sample preparation, and smaller particles with irregular shapes and less-defined edges. Nonetheless, the mAP@IoU50 calculated on 50 random slices resulted in 97% and 82% for the unflawed and flawed electrodes respectively. These results imply that while the model didn't always detect smaller particle fragments of uneven shape that might be uncommon to numerous datasets, (and, hence, under-represented in the training data), it performs sufficiently well in identifying larger particles, both unflawed and flawed or cracked. This can again be confirmed in Figure 2a,b.

After each 2D slice was segmented, these were assembled into a 3D stack with the resampling and filtering procedure described in the methodology, allowing it to be compared in 3D with the segmentation and particle labelling obtained via thresholding, as presented in Figure 3.

The two main differences that can be observed from the labeled images in Figure 3b,c are the fragmented segmentation of the large, cracked particle and the presence of smaller particles. Due to the similarity in grayscale value between flaws and pores, traditional segmentation approaches cannot distinguish between the two clearly. Consequently, the watershed particle separation step may wrongly identify cracks and flaws as pores that run through the particle, dividing it into multiple sections. In contrast, as the model developed here was trained to recognize all particles as a single object, the cracked particle was correctly identified by the computer vision approach as a single entity. This is a vital requirement if cracking within battery materials is to be fully analyzed in an automated

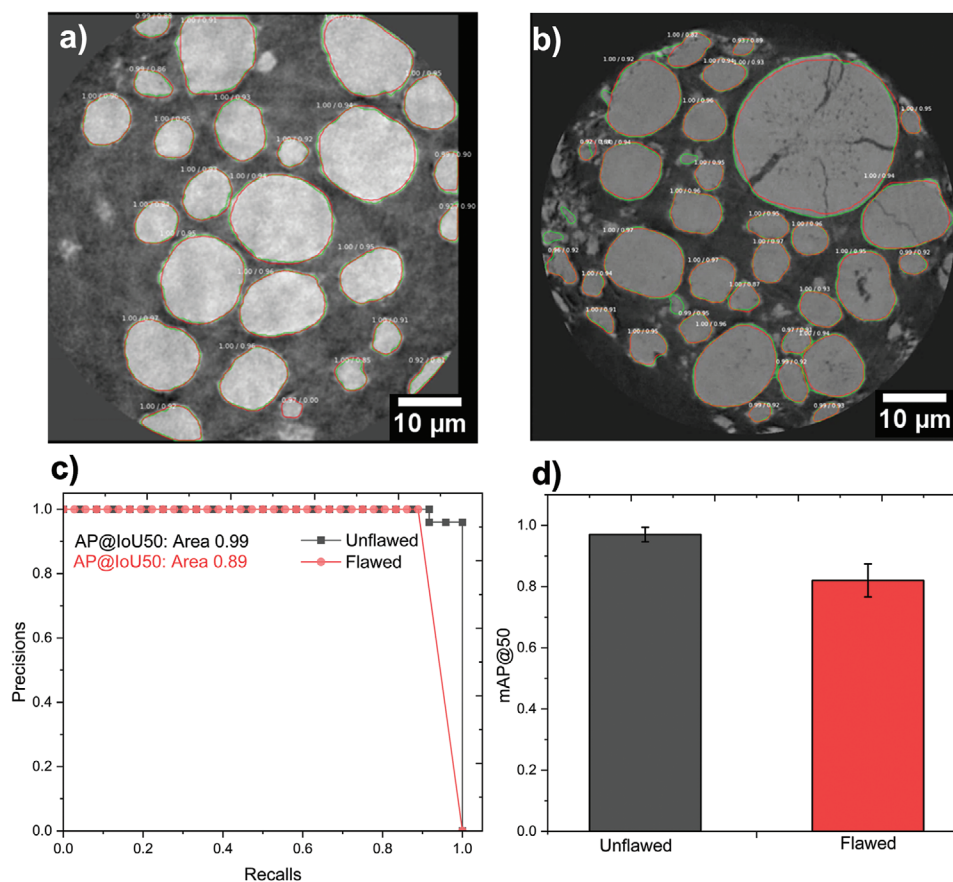


Figure 2. a) Ground truth (green) versus prediction (red) for a slice extracted from the unflawed dataset. b) Ground truth versus prediction for a slice of the flawed dataset. c) Precisions-recalls curve for both slices. d) mAP calculated over 50 random slices at IoU of 50% for the unflawed and flawed datasets.

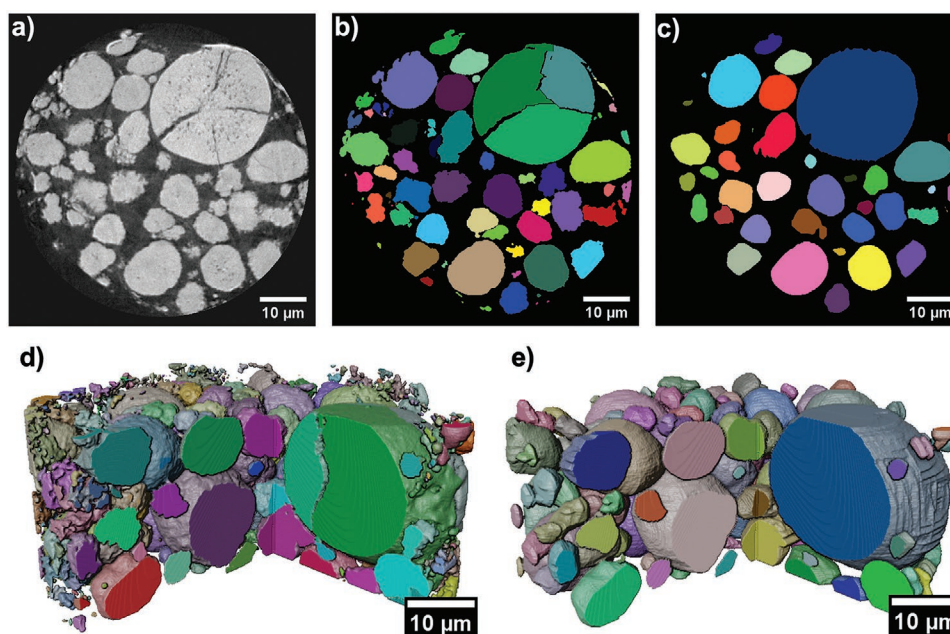


Figure 3. a) Grayscale slice extracted from the flawed tomography dataset. b) Slice extracted from the flawed tomography dataset segmented and labelled with thresholding. c) Slice extracted from the flawed tomography dataset segmented and labelled with the CV approach. d) Volume rendering of the threshold segmentation. e) Volume rendering of the CV segmentation.

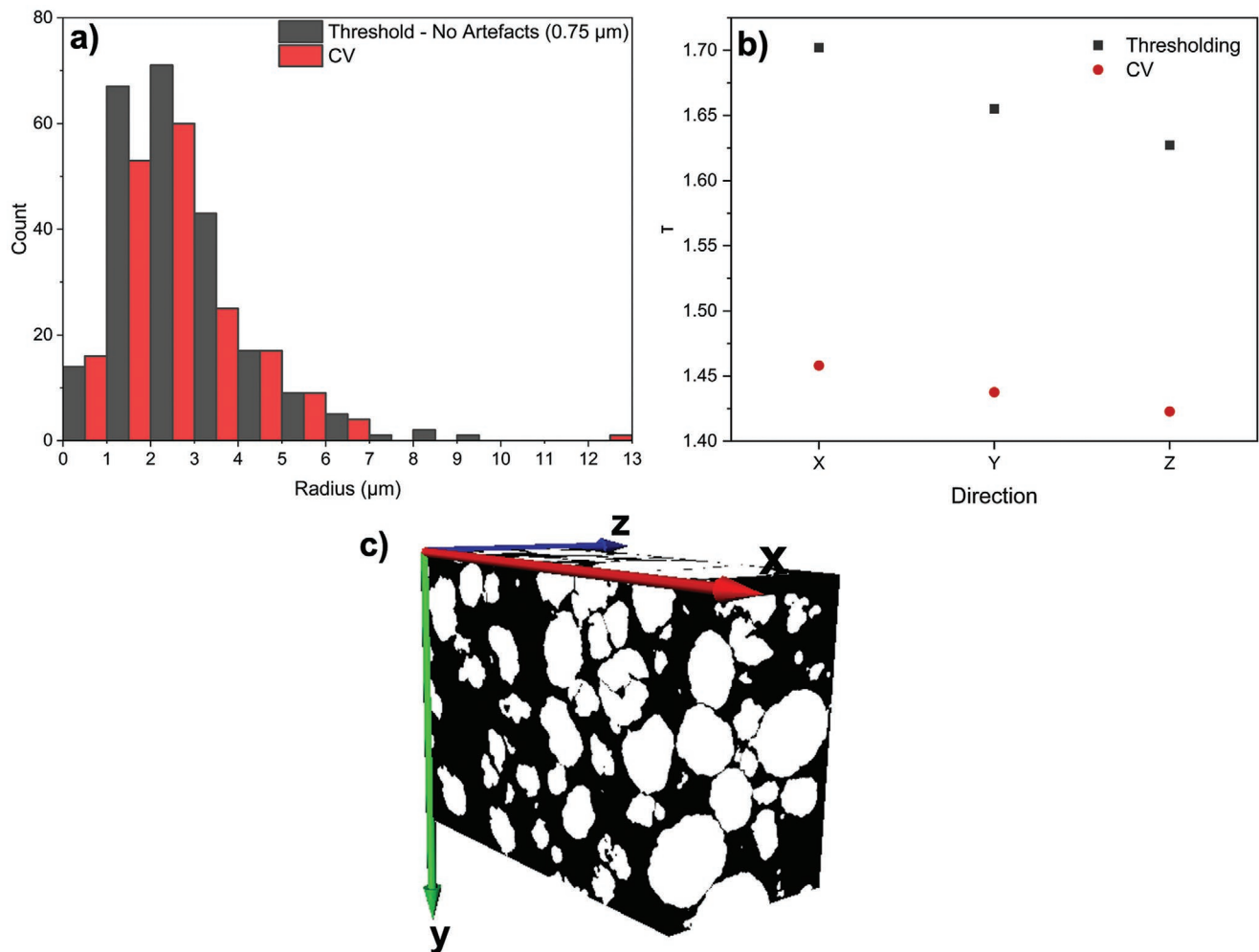


Figure 4. a) PSD calculated for the flawed tomography for threshold and CV approaches. The threshold PSD excludes particles with radii below $0.75 \mu\text{m}$. The bin centers are in the middle of the two columns for each size. b) Tortuosity factor for the thresholding and CV segmentations. c) 3D representation of the three directions with respect to the dataset dimensions.

manner: it allows for classification of each individual particle based on its microstructure as will be presented in the following section. This can also be visualized in the 3D representations in Figure 3d,e. Further comparisons between the thresholding and CV segmentation can be deduced by comparing the particle size distribution (PSD) and tortuosity factor as shown in **Figure 4**.

The PSD presented for the threshold segmentation excludes all particles with radii below $0.75 \mu\text{m}$ as these were regarded as pixel artefacts below the resolution limit that often come as a by-product of thresholding. Interestingly, these are not present in the CV segmentation as small pixel-size artefacts are not detected as objects of interest. The full PSD including the removed artefacts is shown in Figure S8, Supporting Information. The rest of the PSD shows that threshold segmentation detected more particles with radii below $3 \mu\text{m}$. Furthermore, a single particle can be observed at the $12 \mu\text{m}$ radius for the CV segmentation, while three particles can be viewed in the $7\text{--}9 \mu\text{m}$ range for the threshold segmentation: these clearly indicate that the large particle is split in three sub-sections by the watershed separation discussed previously. Mean particle sizes of ≈ 1.0 and

$2.6 \mu\text{m}$ were calculated for the threshold and CV segmentation, respectively, which again confirms that traditional thresholding is more apt at identifying smaller fragments.

The tortuosity factor is also measured on the binary datasets: while there is no distinction between pore and CBD, leading to an underestimation of the value, this can give an indication of fidelity between the different segmentation algorithms.^[28] A reduction in tortuosity factor can also be observed in all three directions, along with pore/CBD phase percentages of 44% and 37% for the CV and threshold segmentations, respectively. While these results indicate that the CV approach omitted some of the smaller particles and fragments, larger particles that are crucial for the purpose of flaw classification and quantification were correctly identified, in line with what is calculated via thresholding. Furthermore, the ability of the CV model to capture flawed particles as a single entity rather than separated objects is essential to correctly capture its bounding box coordinates as will be described in the following section.

After the particles were identified in 2D and a 3D volume was reconstructed from each slice, each particle was labeled

individually using the cc3d package, which also provides the bounding box coordinates in 3D.^[29] These are used to directly crop sub-volumes containing each particle in the original grayscale image.

2.3. Particle Classification

The classifier assigns a score of 0 if the particle is unflawed, and 1 if the particle contains a crack or a flaw. This was trained with an early stopping monitor of 15 epochs set on the validation accuracy; as a result, optimal training and validation accuracies of 93% and 92% were obtained in just over a few minutes as presented in Figure 5a,b.

Further information on the classifier performance is obtained by analyzing the area under the curve (AUC) receiver operating characteristics (ROC) and confusion matrix in Figures 5c,d,

respectively. An AUC of 0.88 indicates that the classifier can correctly distinguish between unflawed and flawed particles. The false positives could be caused by varying grayscale patterns in the core of the particles that might mimic thin hairline cracks, or edge artefacts resulting from the particle masking process used to generate training datasets. On the other hand, false negatives could be caused by the classifier not correctly identifying particles that have very faint flaws and were labelled as unflawed. These issues are common to manual or threshold segmentation as well, where correct identification of flaws is hindered by the resolution limit of the instrument used. Future improvements in image resolution will undoubtedly aid in generating more reliable training data and in turn enhancing classifier performance.

From the previous CV segmentation step, each particle's grayscale image was separated from the rest of the electrode using the 3D masks generated with Mask R-CNN's instance

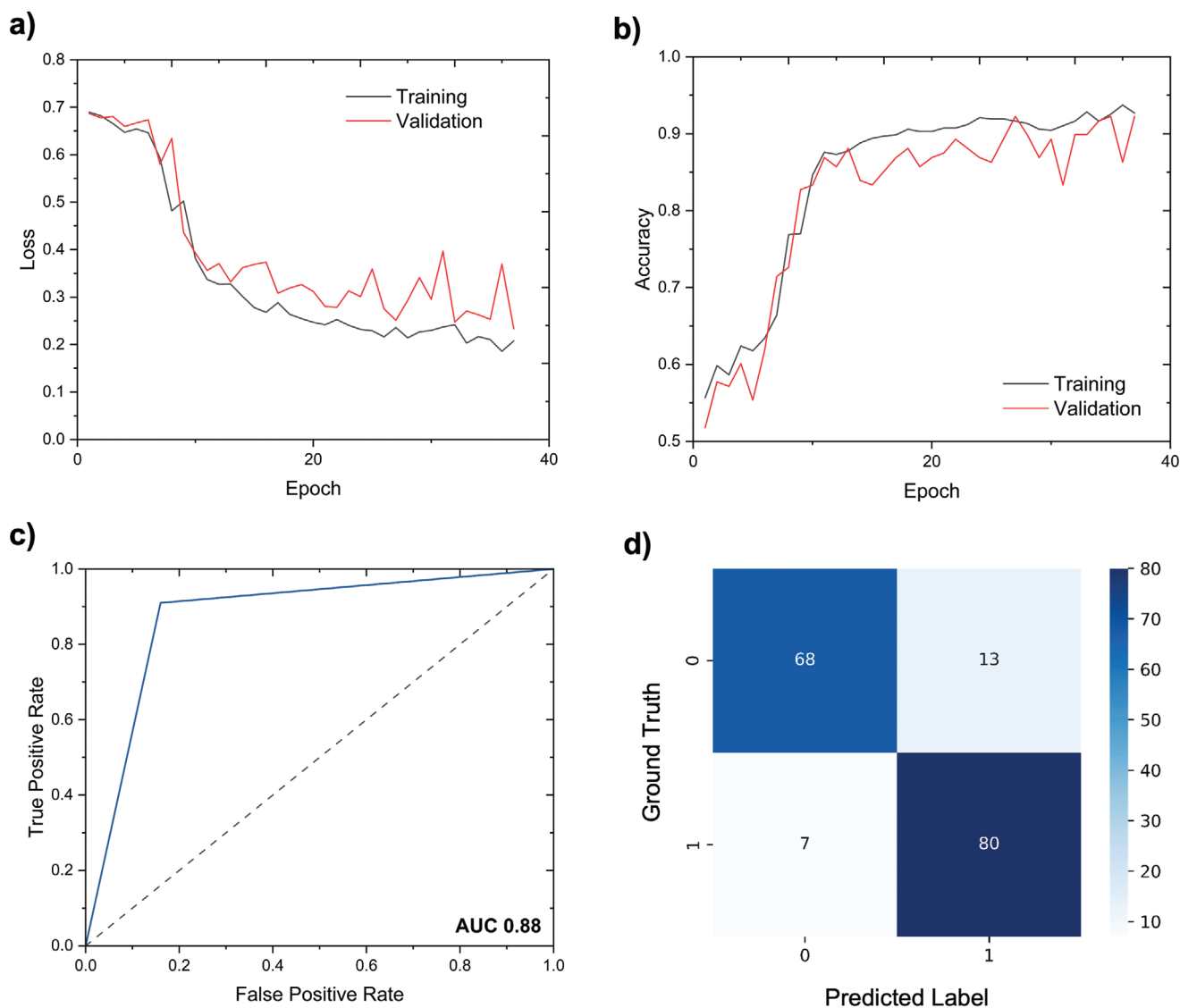


Figure 5. Training and validation a) losses and b) accuracies for the classifier network. c) AUC-ROC curve for the classifier network presenting the true positive and false positive rates. d) Confusion matrix showing classifier performance on validation set.

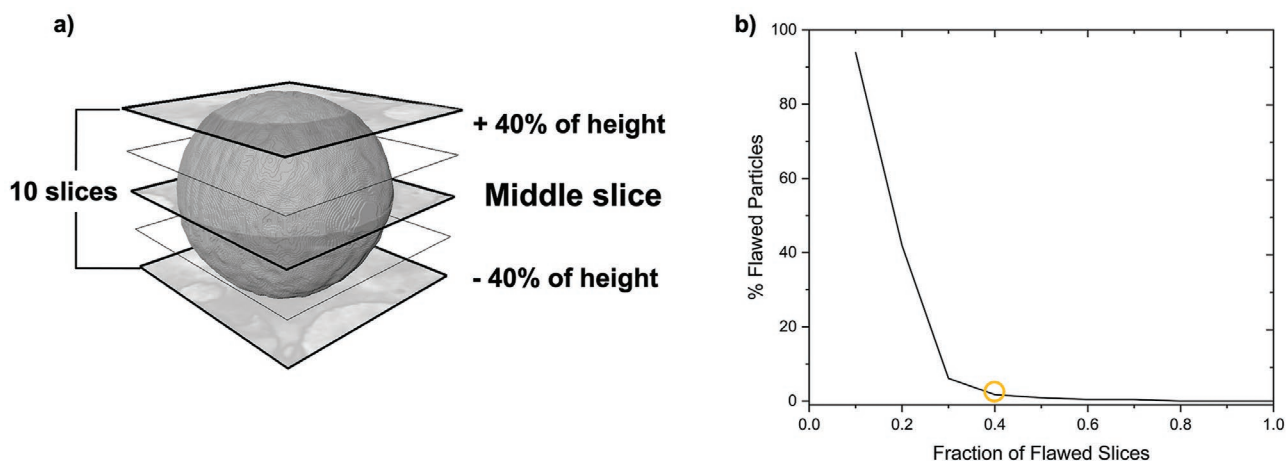


Figure 6. a) Diagram depicting the slicing carried out for each particle prior to classification. b) Change in the percentage of flawed particles as a function of the number of slices considered for a flawed particle. The yellow circle indicates chosen threshold.

segmentation. Ten evenly spaced grayscale slices were extracted throughout 80% of the total height of each particle as shown in Figure 6a.

Each slice was individually classified using the pre-trained classifier: a slice containing a flaw or a crack was assigned a score of 1. A mean particle score was then defined as the mean score from the ten slices. Due to the false positive rate and overall classifier performance presented in Figure 5, the particle was identified as flawed if there were at least 4 slices classified as flawed present. This value was determined by quantifying the percentage of flawed particles as the number of flawed slices considered was increased by 1 for a previously unseen dataset, where the effective number of flawed particles is determined to be negligible by visual examination. A summary of this process is shown in Figure 6b. When one slice containing a flaw was deemed sufficient to consider a particle cracked, over 95% of the particles were classified as flawed, indicating that most of these slices are likely to be false positives. The percentage of particles classified as flawed drops from 6% to 1% when three and four slices respectively were deemed sufficient for a particle to be considered as flawed, confirming that below a threshold of four slices, most of the flawed particles are likely to be false positives. Visual confirmation was also carried out on all the particles detected as flawed and the remaining particles in the electrode dataset. The slicing only occurs in the XY direction: while in theory a crack could be missed were it completely parallel to the slicing plane, this does not occur based on the visual examination of an extensive number of datasets and individual particle slices. For reference, the structure of the classifier is presented in Figure S6, Supporting Information, with sample activation maps presented for each convolutional block, highlighting correct identification of internal flaws and cracks.

The CV segmentation step lasts between 1.0 and 1.5 h depending on the size of the dataset, while the classification process lasts less than a minute for 150–200 particles. While a certain degree of error and inaccuracies may be present at either of these steps, the equivalent process would take exponentially longer were it to be carried out manually. Moreover, the output from the classification step can be utilized for further automated analysis of the nano-CT images.

2.4. Case Studies: Cycled and Flawed Electrodes

As a case study, the segmentation and classifier models were applied to three previously unseen datasets: an uncycled NMC811 electrode, an electrode with the same composition after a single charge to 5 V and an uncycled NMC622 electrode containing numerous flawed particles. A high cut-off voltage is key to unlock higher energy densities of these materials: however, particle cracking hinders long term usability as it accelerates cycle life degradation. These are presented in Figures 7a,d,g, respectively. After cycling, numerous cracked particles appeared in the NMC811 electrode, as shown in Figure 7d. As a first step, a 3D CV segmentation is carried out on each dataset and each particle is labeled individually.

Inter-granular cracking within NMC811 particles is thought to depend on the strain caused by the reduction and subsequent collapse of the interlayer spacing at high delithiation on primary and secondary particles.^[30]

It is clear from the volume renderings in Figure 7 that the CV segmentation yields an excellent result; while some artefacts are present on smaller particles (e.g., below 2–3 μm radius), as described previously, most mid-sized and large particles (e.g., above 4 μm radius) are correctly segmented. While the edges of some of the smaller particles contain slice-like artefacts, these generally do not impede the bounding box extraction process and subsequent classification. Using the numerical threshold of flawed particles determined previously, the number of flawed and cracked particles are counted for each dataset and presented in Table 1.

While a certain degree of error is certainly associated with every classification process, the relatively high precision and recall of the classifier, and the rigorous particle slicing presented in the previous section, indicate that the model can rapidly and accurately identify microstructural trends within electrode nano-CT datasets. The percentage of cracked particles increased from a negligible 1.7% to 30.8% for the cycled electrodes. The automated nature of the process and the relatively short time required for classification are a great advantage; manually identifying cracked particles by scrolling through each individual slice can be time-consuming and

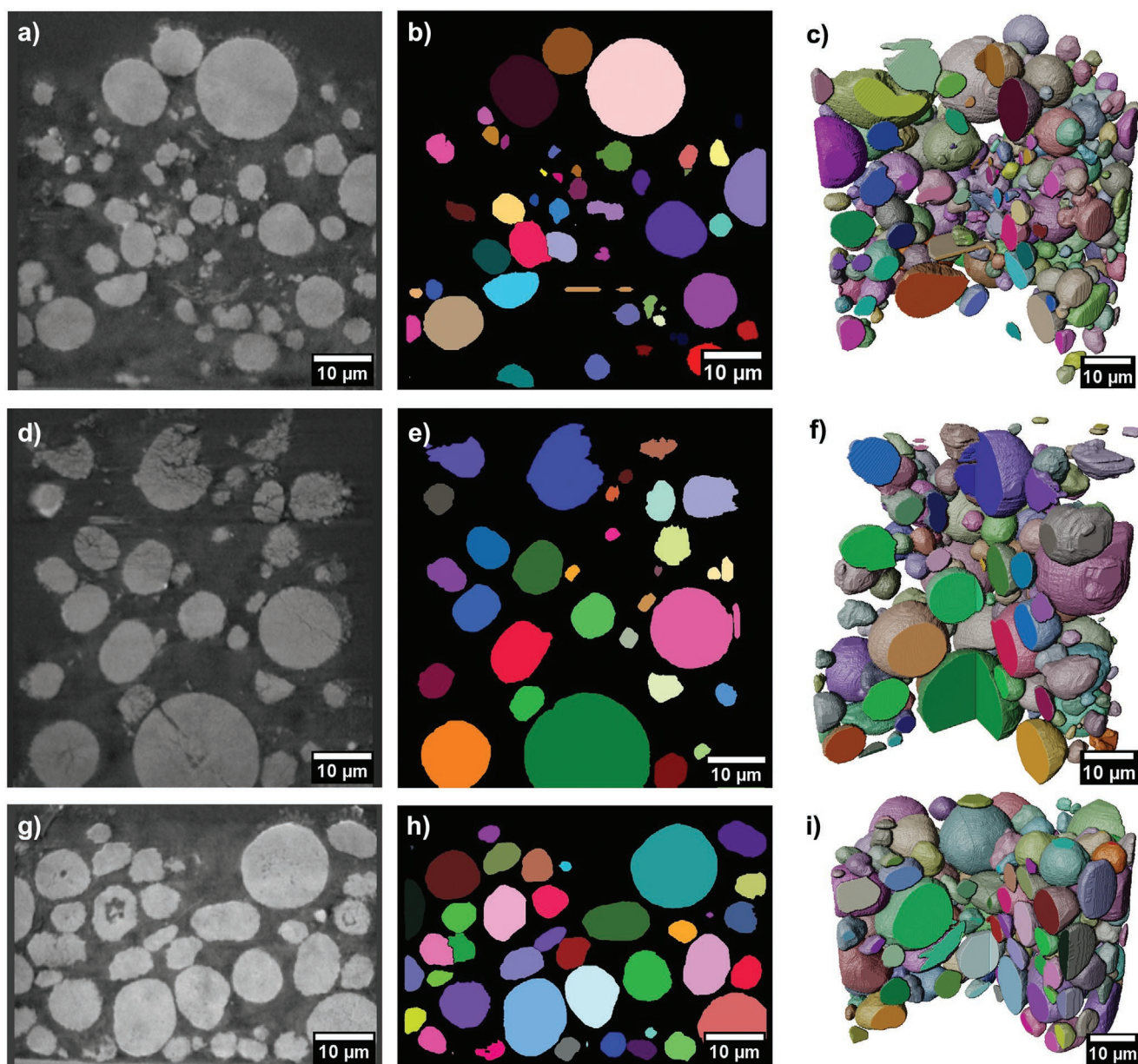


Figure 7. a,d,g) Virtual slices containing a grayscale image from the uncycled NMC811, 5 V NMC811 and flawed NMC622 datasets. b,e,h) Virtual slices showing the CV segmentation for the uncycled, 5 V and flawed datasets. c,f,i) Volume renderings with individually labelled particles for the CV segmentation for the uncycled, 5 V and flawed datasets.

inexact, as well as prone to human errors and judgement biases. Interestingly, the model excels at recognizing flawed particles with a different flaw morphology as well; this is due to the broad variety of images provided for training the classifier. Examples of such features are presented in Figure S7, Supporting Information.

2.5. 3-Phase Segmentation: Proof of Concept

Once each particle is classified, numerous image-based operations can be carried out on each of the classes. While improvements in image collection and segmentation accuracy are

required to fully automate this process and apply it to entire electrode datasets, a proof of concept 3-phase segmentation is carried out on flawed particles as presented in Figure 8. Again, separating the similar grayscale features of cracks from pores or

Table 1. Number and percentage of flawed particles detected for the uncycled, 5 V and flawed NMC622 datasets.

Dataset	Unflawed	Flawed	% Flawed
Uncycled	225	4	1.7
5V	110	49	30.8
Flawed NMC622	99	48	32.6

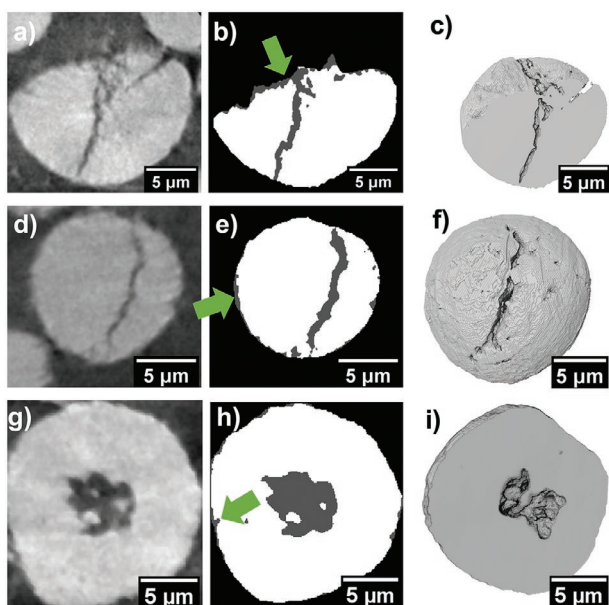


Figure 8. Grayscale slice, 3-phase segmentation and volume rendering for a–f) cracked particles extracted from the 5 V dataset and g–i) a flawed particle extracted from the flawed NMC622 dataset. Green arrow indicates edge artefacts.

voids between the particles is a laborious and difficult process for manual segmentation; however, if cracks can be accurately segmented as a separate phase from the void space it allows for valuable analysis of the size, provenance, and orientation of cracks, which can lead to significant insight into the microstructural effects of degradation of battery electrodes. Therefore, automation of this process is highly desirable as it can allow analysis of the many thousands of particles required for statistical significance, which is currently not possible with manual segmentation or methods that only capture a small number of particles, such as single tomograms or cross-sectional SEM imaging.

To distinguish the pixels belonging to the flawed phase, the CV segmentation is overlaid with a mask obtained with thresholding where the flaw contours are contained in the segmentation. By assigning unique numerical values to pore/flaw/crack and solid phases, the flaw can be segmented independently from the rest by multiplying the different components. An example of such masks is presented in Figure S9, Supporting Information. The flaw volume or volume fraction can also be calculated by multiplying the number of flawed pixels with the image pixel resolution. A downside of this approach is that a mismatch between the two masks will create edge artefacts as shown in Figure 8b,e,h. Furthermore, issues may arise when exceptional features are present in the analyzed dataset but not in the training sets, leading to uncertain segmentation results as shown in Figure S9, Supporting Information. While this does not seem to impede the overall classification of the particle, the presence of unusual features may hinder this approach to segment flaws. Nonetheless, this is the first time to the authors' knowledge where an autonomous process segments, classifies and finally separates different elements in an electrode and it is eminently possible to improve with additions to the training data sets and automated improvement of segmentation artefacts.

Potential avenues for improving the 3-phase segmentation range from implementing automated erosion and dilation mechanisms to eliminate boundary artefacts to advances in image acquisition. Improvements in image resolution and quality will enable more accurate imaging and segmentation of finer hairline cracks, as well as edges between particles and the CBD where unique features can often confuse the initial CV segmentation step. Further improvements in the detection of edges could also be obtained by utilizing newer instance segmentation models (e.g., Pointrend^[31]) or by increasing the training sets to encompass a wider collection of features; the latter approach however might result in an extremely laborious process to manually segment a large number of training sets. Alternatively, the CV segmentation output could be manually improved and recursively utilized for a further round of training, refining the model's knowledge, and encompassing all the different families of features that could occur in the data.

While this proof of concept segmentation is relatively simple, it opens the opportunities for further analysis of cracks and flaws, for example by studying their internal surface areas and orientations.^[32] Furthermore, the crack severity could be estimated by measuring the distance of the crack to the particle surface. After labeling and classification, the electrode could be spatially reconstructed, and the flaw distribution could be spatially localized throughout the depth of the electrode. All these metrics could then be related to the electrochemical performance of the electrode. Automated image quantification and classification tasks are gaining increasing interest in the field of Li-ion battery research, as they allow for rapid insight in electrode morphology and microstructural evolution.^[33,34] The development of the concepts here presented will undoubtedly provide a valuable addition for the field of electrode research and beyond.

3. Conclusion

While X-ray CT enables non-destructive multi-length scale imaging of battery electrodes, traditional grayscale-based segmentation approaches are hindered by their failure to distinguish between different features with similar intensity values. Here, we present a novel approach that combines an instance segmentation network with a convolutional classifier to locate and classify NMC particles in nano-CT tomograms in 3D. This allows for accurate and effective identification of a range of different morphologies, particle classification and 3-phase segmentation in 3D.

The instance segmentation network operates in 2D by identifying individual particles in each slice composing a full electrode dataset. The slices are successively reconstructed in 3D with a series of morphological operations to smooth out any artefacts that may have been generated because of this process. To ensure that the model generalizes well on unseen data, an automated method was developed to generate COCO-style annotations and exponentially increase the amount of training and validation sets while greatly reducing the time required.

After segmentation, each particle is individually labelled and sliced in ten sections through its height. These slices are then classified using the second network to detect whether the particle contains a manufacturing flaw or a crack. This enables us to rapidly obtain useful statistics on the electrode

morphology and its variations as a result of synthesis or cycling. As a proof of concept, a 3-phase segmentation is also presented, where flaws and cracks are extracted as separate pixel values in the label images, which will lead to advanced automated analysis of the effects of degradation on battery materials.

The modular nature of the two networks working synergistically will enable adapting the system for a multitude of case-studies and materials across different length-scales where sizeable training data is available.

4. Experimental Section

X-Ray CT Data Collection: The nano-CT datasets used to train the Mask R-CNN model were pillar samples prepared from electrode sheets using a laser machining procedure to mill 1 mm electrode disks to diameters between 80 and 100 μm . The full description of the sample preparation can be found elsewhere.^[35] The datasets were collected on a lab-based X-ray CT system, Ultra 810 (Carl Zeiss Inc) in absorption contrast mode, using a pixel binning of 1, resulting in a pixel size of 64 nm. The exposure time varied depending on the overall diameter of the sample, ranging between 30–60 s per projection. The radiographs were reconstructed using the commercially available Zeiss XMReconstructor (Carl Zeiss Inc) with a filtered back-projection algorithm. Reconstruction yields a .txm file that can be opened with Avizo 2019 (Thermo Fisher Scientific). These .txm datasets were converted into 2D .tiff stacks for the annotation generation steps.

Coin Cell Cycling: 15 mm discs of NMC811 (NEI NANOMYTE BE-50E cast NMC811) were employed in CR-2032 type coin cells assembled in an argon-filled glovebox, with an active material fraction of 90 wt%. Lithium metal was used as the counter electrode. Due to the instability of electrolyte additives at higher voltages, LP57 (1 M solution of LiPF₆ in EC/EMC = 3/7 (v/v)) was used. Celgard separator was used as separator (2400; Celgard). Samples were cycled using a BCS805 (BioLogic) coin cell cycler and were charged to 5 V using a current rate of 0.02C, which is an aggressive high-voltage protocol chosen to induce cracking. The cells were then disassembled in an argon-filled glovebox where the electrodes were washed in dimethyl carbonate (DMC) and left to dry before exposing them to air for ex situ analysis. The cycling curve is presented in Figure S1, Supporting Information.

Label Generation and Mask R-CNN Training: All machine learning training, validation, and application algorithms were run on a local workstation with an Intel Xeon Gold 6134 CPU, NVIDIA Quadro P5000 running Windows Server 2016 Standard. The training and validation sets for the Mask R-CNN model were segmented with a combination of grayscale thresholding and manual paint brush tools in Avizo 2019: this was to ensure that each flaw or crack is segmented as the solid phase. The labels and grayscale images were exported to 8-bit 2D slices prior to the label generation step. All the following steps were carried out using Python 3.7. Most of the tools developed are available on our public GitHub repository. The spatial location of each particle was converted into a COCO-style annotation file using a custom Python script. The script loads individual 2D grayscale slices and their corresponding binary label image and separates these into training and validation subsets by copying them in separate folders. The spatial coordinates of each particle in 2D, generated from the segmentation outlines, were inscribed in a .json file. Separate folders and .json files were produced for training and validation sets and named in the correct style for loading within Mask R-CNN. The .json file is structured in the standard format that most computer vision packages can read and an example of the key features is provided in Figure S2, Supporting Information.

Particle detection in 2D was carried out using Mask R-CNN, a region-based convolutional network widely used for object detection. The model operated by using a region proposal network based on an established backbone to identify the possible locations of each object in the image. Successively, bounding boxes were predicted for each of the proposed regions. Finally, the model segmented the individual boundaries of each of the detected

objects. In this work, the model used a Resnet101 backbone. To increase the object-recognition abilities of the model, it was initialized using the weights of the large-scale COCO dataset. The head of the model was then cyclically trained using the annotations generated for the NMC datasets. The model was trained for 450 epochs using 5 nano-CT datasets. Training of the Mask R-CNN component of the model took ≈ 75 hours to train on a dedicated GPU-enabled workstation with system specifications described previously. Each slice was rotated and orthogonally flipped to increase the variability of the data and reduce similarity between neighboring slices. An example is presented in Figure S3, Supporting Information. A learning rate of 0.0001 was used.

To reconstruct the 2D segmented slices into a 3D volume, the data were resampled in all three directions (XY, XZ, YZ), segmented and re-combined in one 3D dataset. An example of the resampling process is presented in Figure S4, Supporting Information. To smooth out artefacts due to the 2D nature of the slice detection, a series of morphological operations such as erosion, hole removal and dilation were applied in series to the data. An example of the resulting data after these operations can also be viewed in Figure S5, Supporting Information. After filtering, the particles were separated in 3D using a watershed algorithm and the spatial coordinates of each particle were extracted using the connected-components-3d package (cc3d).

Classifier Training and Validation: The classifier was built following a VGG16 architecture and was assembled using Tensorflow 2.2.0. A diagram highlighting the number of convolutional filters used is presented in Figure S6, Supporting Information. Two convolutional layers per number of filters were followed by a rectified linear unit (ReLU) activation before being fed into a maximum pooling layer with a stride of 2. A dropout of 10% was used to improve overall accuracy. A final dense layer fed the result into an output layer with a sigmoid activation function. The training and validation sets for the classifier consisted of 2D grayscale slices of masked particles and were extracted from a collection of previously gathered nano-CT datasets. Over the past decade, we have collected an extensive library of nano-CT data, some of which are available via public repositories.^[36,37] Manual thresholding was used to create a binary mask that encompasses the entirety of each particle in 3D. The particles were then exported as 3D .tiff stacks and later re-sliced in 2D. An example of such slices is shown in Figure S6, Supporting Information. The classifier was trained on 755 particle slices subdivided into two classes, unflawed, and flawed: any particle with visible cracks or flaws was assigned to the latter phase. The slices were resized to 128 \times 128 pixels for the input layer dimensions of the classifier. The slices were augmented with a series of operations such as rotation, width/height shift, zoom range, and orthogonal flipping to increase variability between the slices. An early stopping monitor interrupted the training when no gains were detected in the validation accuracy after 15 epochs. Classifier training stopped after ≈ 40 epochs, with training and validation accuracies of 93% and 92% respectively. The training process took <10 min to complete. The classifier will be provided in our public repository and can be loaded in Keras/Tensorflow.

At the end of the particle detection step, each particle mask obtained using Mask R-CNN provides spatial coordinates of the particles in 3D. The spatial coordinates of each particle bounding box were used to crop the particles from the original grayscale volume and were fed into the classifier after resizing. Some slice-like artefacts were generated because of inexact instance segmentation. These were eliminated using a Mahalanobis multi-variate outlier detection algorithm.^[38] As some of the particles were located on the edge of the nano-CT dataset, the resulting cropped bounding box may only represent a partial volume. Hence, arrays with >20% of the surface of a slice covered by boundary pixels were excluded as partial/incomplete particles.

Image Visualization and Analysis: 3D visualization and PSD calculations of the thresholded and CV segmentations were carried out with Avizo 2019. The tortuosity factor was calculated using the TauFactor plugin in Matlab on an internal sub-volume measuring 605 \times 761 \times 366 pixels.^[39]

Flaw Segmentation: Prior to classification, the particle slices were resized to 128 \times 128 pixels as required by the model input layer. Classification is run on ten slices selected to be within 80% of the total height of the electrode. To classify a particle as flawed, the mean score returned by the classification must be ≥ 0.4 .

3-phase segmentation was carried out by overlaying the particle mask obtained via Mask R-CNN, where flaws were segmented as part of the active material phase, and a threshold segmentation carried out on the masked particle slice. By assigning distinct numerical values to the background and particle masks and multiplying the values of the two segmentations, the area of the masks where particle and flaw overlap will result in a unique numerical value that identifies the flaw. Threshold segmentation was carried out using the OpenCV package and using the triangle and binary modes. This part of the algorithm is provided in the public repository.

Supporting Information

Supporting Information is available from the Wiley Online Library or from the author.

Acknowledgements

The authors would like to acknowledge the Faraday Institution grants (EP/S003053/1, FIRG016, FIRG024 and FIRG025), and InnovateUK. PRS would like to acknowledge (CiET1718/59) and DJLB the Royal Academy of Engineering funding for supporting their respective Research Chairs and Senior Research Fellowships scheme (RCSRF2021/13/53).

Conflict of Interest

The authors declare no conflict of interest.

Data Availability Statement

The data that support the findings of this study are available from the corresponding author upon reasonable request.

Keywords

computer vision, convolutional networks, lithium-ion batteries, mask R-CNN, nano X-ray tomography

Received: July 8, 2022
Revised: August 23, 2022
Published online:

- [1] J. Tarascon, M. Armand, *Nature* **2001**, 414, 359.
- [2] J. Xu, S. Dou, H. Liu, L. Dai, *Nano Energy* **2013**, 2, 439.
- [3] O. Badmos, A. Kopp, T. Bernthaler, G. Schneider, *J. Intell. Manuf.* **2020**, 31, 885.
- [4] J. Dahn, G. M. Ehrlich, in *Handb. Batter.*, McGraw Hill Professional, Access Engineering **2002**, 26.1.
- [5] B. Scrosati, J. Garche, *J. Power Sources* **2010**, 195, 2419.
- [6] P. Yan, J. Zheng, M. Gu, J. Xiao, J.-G. Zhang, C.-M. Wang, *Nat. Commun.* **2017**, 8, 14101.
- [7] Z. Zhang, S. Said, K. Smith, R. Jervis, C. A. Howard, P. R. Shearing, D. J. L. Brett, T. S. Miller, *Adv. Energy Mater.* **2021**, 11, 2101518.
- [8] J. Zhu, L. Lu, K. Zeng, *ACS Nano* **2013**, 7, 1666.
- [9] H. Liu, J. M. Foster, A. Gully, S. Krachkovskiy, M. Jiang, Y. Wu, X. Yang, B. Protas, G. R. Goward, G. A. Botton, *J. Power Sources* **2016**, 306, 300.
- [10] D. P. Finegan, A. Vamvakeros, L. Cao, C. Tan, T. M. M. Heenan, S. R. Daemi, S. D. M. Jacques, A. M. Beale, M. Di Michiel, K. Smith, D. J. L. Brett, P. R. Shearing, C. Ban, *Nano Lett.* **2019**, 19, 3811.
- [11] X. Lu, A. Bertei, D. P. Finegan, C. Tan, S. R. Daemi, J. S. Weaving, K. B. O'Regan, T. M. M. Heenan, G. Hinds, E. Kendrick, D. J. L. Brett, P. R. Shearing, *Nat. Commun.* **2020**, 11, 2079.
- [12] E. N. Landis, D. T. Keane, *Mater. Charact.* **2010**, 61, 1305.
- [13] J. Li, Z. Zhou, Z. Luo, Z. He, J. Zheng, Y. Li, J. Mao, K. Dai, *Sustainable Mater. Technol.* **2021**, 29, e00305.
- [14] Y. Mao, X. Wang, S. Xia, K. Zhang, C. Wei, S. Bak, Z. Shadike, X. Liu, Y. Yang, R. Xu, P. Pianetta, S. Ermon, E. Stavitski, K. Zhao, Z. Xu, F. Lin, X. Q. Yang, E. Hu, Y. Liu, *Adv. Funct. Mater.* **2019**, 29, 1900247.
- [15] A. Van Bommel, R. Divigalpitiya, *J. Electrochem. Soc.* **2012**, 159, A1791.
- [16] X. Lu, X. Zhang, C. Tan, T. M. M. Heenan, M. Lagnoni, K. O'Regan, S. Daemi, A. Bertei, H. G. Jones, G. Hinds, J. Park, E. Kendrick, D. J. L. Brett, P. R. Shearing, *Energy Environ. Sci.* **2021**, 14, 5929.
- [17] P. Li, Y. Zhao, Y. Shen, S. Bo, *J. Phys. Energy* **2020**, 2, 022002.
- [18] K. A. Severson, P. M. Attia, N. Jin, N. Perkins, B. Jiang, Z. Yang, M. H. Chen, M. Aykol, P. K. Herring, D. Fraggedakis, M. Z. Bazant, S. J. Harris, W. C. Chueh, R. D. Braatz, *Nat. Energy* **2019**, 4, 383.
- [19] Y. Zhang, Q. Tang, Y. Zhang, J. Wang, U. Stimming, A. A. Lee, *Nat. Commun.* **2020**, 11, 6.
- [20] X. Chen, L. Ye, Y. Wang, X. Li, *Adv. Intell. Syst.* **2019**, 1, 1900102.
- [21] G. Dong, X. Zhang, C. Zhang, Z. Chen, *Energy* **2015**, 90, 879.
- [22] L. Petrich, D. Westhoff, J. Feinauer, D. P. Finegan, S. R. Daemi, P. R. Shearing, V. Schmidt, *Comput. Mater. Sci.* **2017**, 136, 297.
- [23] S. Müller, C. Sauter, R. Shunmugasundaram, N. Wenzler, V. De Andrade, F. De Carlo, E. Konukoglu, V. Wood, *Nat. Commun.* **2021**, 12, 6205.
- [24] Z. Jiang, J. Li, Y. Yang, L. Mu, C. Wei, X. Yu, P. Pianetta, K. Zhao, P. Cloetens, F. Lin, Y. Liu, *Nat. Commun.* **2020**, 11, 2310.
- [25] K. He, G. Gkioxari, P. Dollar, R. Girshick, *IEEE Trans. Pattern Anal. Mach. Intell.* **2020**, 42, 386.
- [26] T. Y. Lin, M. Maire, S. Belongie, J. Hays, P. Perona, D. Ramanan, P. Dollár, C. L. Zitnick, *Lect. Notes Comput. Sci.* **2014**, 8693 LNCS, 740.
- [27] A. Dutta, A. Zisserman, in *Proc. 27th ACM Int. Conf. Multimed.*, ACM, New York, NY, USA **2019**.
- [28] S. R. Daemi, C. Tan, T. Volkenandt, S. J. Cooper, A. Palacios-Padros, J. Cookson, D. J. L. Brett, P. R. Shearing, *ACS Appl. Energy Mater.* **2018**, 1, 3702.
- [29] W. Silversmith, cc3d: Connected components on multilabel 3D & 2D images, <https://zenodo.org/record/5719536#.YxcaW-ZMKHt>, (accessed: September 2022).
- [30] T. M. M. Heenan, A. Wade, C. Tan, J. E. Parker, D. Matras, A. S. Leach, J. B. Robinson, A. Llewellyn, A. Dimitrijevic, R. Jervis, P. D. Quinn, D. J. L. Brett, P. R. Shearing, *Adv. Energy Mater.* **2020**, 10, 2002655.
- [31] A. Kirillov, Y. Wu, K. He, R. Girshick, in *2020 IEEE/CVF Conf. Comput. Vis. Pattern Recognit.*, IEEE **2020**.
- [32] Z. Wu, T. Yang, Z. Deng, B. Huang, H. Liu, Y. Wang, Y. Chen, M. C. Stoddard, L. Li, Y. Zhu, *Integr. Mater. Manuf. Innov.* **2019**, 8, 559.
- [33] A. Wade, T. M. M. Heenan, M. Kok, T. Tranter, A. Leach, C. Tan, R. Jervis, D. J. L. Brett, P. R. Shearing, *Npj Mater. Degrad.* **2022**, 6, 44.
- [34] X. Lu, S. R. Daemi, A. Bertei, M. D. R. Kok, K. B. O'Regan, L. Rasha, J. Park, G. Hinds, E. Kendrick, D. J. L. Brett, P. R. Shearing, *Joule* **2020**, 4, 2746.
- [35] J. J. Bailey, T. M. M. Heenan, D. P. Finegan, X. Lu, S. R. Daemi, F. Iacoviello, N. R. Backeberg, O. O. Taiwo, D. J. L. Brett, A. Atkinson, P. R. Shearing, *J. Microsc.* **2017**, 267, 384.
- [36] T. M. M. Heenan, A. Jnawali, M. D. R. Kok, T. T. G. Tranter, C. Tan, A. Dimitrijevic, R. Jervis, D. J. Brett, P. R. Shearing, RDR UCL **2020**, https://rdr.ucl.ac.uk/collections/Data_Collection_for_an_Advanced_Datasheet_on_18650_Li-ion_Batteries_with_Nickel-Rich_NMC811_Cathodes_and_Graphite-Silicon_Anodes/4994651.
- [37] F. L. E. Usseglio-Viretta, A. Colclasure, A. N. Mistry, K. P. Y. Claver, F. Pouraghajan, D. P. Finegan, T. M. M. Heenan, D. Abraham, P. P. Mukherjee, D. Wheeler, P. Shearing, S. J. Cooper, K. Smith, *J. Electrochem. Soc.* **2018**, 165, A3403.
- [38] T. R. Etherington, *PeerJ* **2021**, 9, e11436.
- [39] S. J. Cooper, A. Bertei, P. R. Shearing, J. A. Kilner, N. P. Brandon, *SoftwareX* **2016**, 5, 203.